INTERNATIONAL JOURNAL FOR NUMERICAL METHODS IN FLUIDS
Int. J. Numer. Meth. Fluids 2008; **57**:929–949
Published online 27 November 2007 in Wiley InterScience (www.interscience.wiley.com). DOI: 10.1002/fld.1662

Genuinely multidimensional characteristic-based scheme for incompressible flows

S. E. Razavi, K. Zamzamian*,† and A. Farzadi

School of Mechanical Engineering, University of Tabriz, Tabriz, Iran

SUMMARY

This paper presents a novel multidimensional characteristic-based (MCB) upwind method for the solution of incompressible Navier–Stokes equations. As opposed to the conventional characteristic-based (CB) schemes, it is genuinely multidimensional in that the local characteristic paths, along which information is propagated, are used. For the first time, the multidimensional characteristic structure of incompressible flows modified by artificial compressibility is extracted and used to construct an inherent multidimensional upwind scheme. The new proposed MCB scheme in conjunction with the finite-volume discretization is employed to model the convective fluxes. Using this formulation, the steady two-dimensional incompressible flow in a lid-driven cavity is solved for a wide range of Reynolds numbers. It was found that the new proposed scheme presents more accurate results than the conventional CB scheme in both their first- and second-order counterparts in the case of cavity flow. Also, results obtained with second-order MCB scheme in some cases are more accurate than the central scheme that in turn provides exact second-order discretization in this grid. With this inherent upwinding technique for evaluating convective fluxes at cell interfaces, no artificial viscosity is required even at high Reynolds numbers. Another remarkable advantage of MCB scheme lies in its faster convergence rate with respect to the CB scheme that is found to exhibit substantial delays in convergence reported in the literature. The results obtained using new proposed scheme are in good agreement with the standard benchmark solutions in the literature. Copyright © 2007 John Wiley & Sons, Ltd.

Received 14 May 2007; Revised 6 October 2007; Accepted 8 October 2007

KEY WORDS: incompressible flow; artificial compressibility; Navier–Stokes equations; multidimensional characteristics; compatibility equations; Mach ellipse

*Correspondence to: K. Zamzamian, Mechanical Engineering Department, Tabriz University, 29 Bahman Bolvar, Emam Khomeyni Ave. 5166616471, Tabriz, Iran.
†E-mail: k_zamzamian@yahoo.com

Contract/grant sponsor: University of Tabriz

1. INTRODUCTION

The concept of artificial compressibility was first introduced by Chorin [1]. With this idea, the continuity and momentum equations are coupled to each other and it is possible to use pseudo-time marching methods for obtaining steady-state solutions. Meanwhile, the nature of incompressible flow equations is changed to hyperbolic one. In pseudo-time marching, the addition of artificial compressibility has no effect on the steady-state results. However, it may affect the convergence process [2]. In pseudo-time marching, the numerical waves created are used for propagating information throughout the solution domain and driving the divergence of velocity to zero. Different numerical schemes have been used for discretization of artificial compressibility equations. Among them, Farmer *et al.* have used a central scheme with Jameson's artificial viscosity to prevent the pressure–velocity decoupling [3]. The discretization schemes and solvers developed for artificial compressibility have many similarities with the methods developed for compressible flows. Many researchers used Godunov-type schemes to discretize the equations of artificial compressibility. Rogers and Kwak [4], Liu *et al.* [5], Kallinderis and Ahn [6] and Yuan [7] used Roe's flux difference splitting scheme for solution of incompressible flow fields. Their Roe's averaging approach was applied to artificial compressibility equations and obtained fluxes in finite-volume discretization are functions of artificial compressibility parameter. Traditionally, the method of characteristics is used primarily for compressible flow calculations. By introducing the pseudo-time derivative in Chorin's formulation, it is possible that the incompressible flow equations be solved by a similar method of characteristics. For the first time Drikakis *et al.* used one-dimensional characteristic relations to calculate the convective fluxes in finite-volume discretization for two-dimensional incompressible flow in a curvilinear coordinate system on structured grids [8]. The method was developed for three-dimensional flows [9] and further developed to incorporate multigrid techniques [10].

The above-mentioned method was extended by Zhao *et al.* for simulation of incompressible flows and convection heat transfer on unstructured two- and three-dimensional grids [11–15]. Flow variables are calculated along characteristics paths in the direction normal to the surface of a control volume and their initial values are interpolated based on the signs of the corresponding characteristic speeds. The characteristic-based (CB) scheme has been used for a broad range of incompressible flow simulations. Siong *et al.* used a CB implicit finite-volume method for calculating incompressible flow in porous media on unstructured grids [16]. Drikakis and Shapiro applied the artificial compressibility method for solving flows with various densities by using a locally one-dimensional characteristic scheme [17, 18]. Other case studies about using the CB schemes in conjunction with artificial compressibility for modeling incompressible flow can be found in References [19–23].

In all of the examples in the literature, the CB schemes for artificial compressibility equations are constructed under the assumption of locally one-dimensional flow in specific directions. All extensions of CB upwind schemes to two and three dimensions ignore the multidimensional nature of flow and advance the solution by 'splitting' that is to say, through a sequence of one-dimensional operators. To take into account the real multidimensional nature of flow, it is necessary to devise methods that consider the actual directions in which information is propagated. Different ideas have been proposed for the definition of genuinely multidimensional schemes for compressible Euler equations such as [24–29], whereas in the case of incompressible flows it has not yet been accomplished because of the difficulties that appear in mathematical characteristics of artificial compressibility equations. It is found from the literature that all of the CB schemes for incompressible flows with artificial compressibility use one-dimensional characteristic relations that

DOI: 10.1002/fld

exhibit substantial delays in terms of convergence in certain studies [23, 30, 31]; they also do not obey the real physical nature of flow. In this study, we derived for the first time, the mathematical structure of two-dimensional characteristics for incompressible flow equations in conjunction with artificial compressibility. Using derived compatibility relations, a genuinely upwind scheme for two-dimensional incompressible viscous flows is presented. The new scheme is applied for two-dimensional lid-driven cavity flow for a wide range of Reynolds numbers, in order to show its ability. Detailed results in comparison with the conventional centered and CB schemes are presented.

2. CHARACTERISTIC STRUCTURE FOR TWO-DIMENSIONAL INCOMPRESSIBLE FLOWS

To derive the characteristic relations of incompressible flows, their corresponding 'Euler equations' are considered [11]. These equations modified by artificial compressibility for deriving two-dimensional characteristic structures are

$$\begin{aligned} \frac{\partial p}{\partial t}+\beta\frac{\partial u}{\partial x}+\beta\frac{\partial v}{\partial y}&=0\\ \frac{\partial u}{\partial t}+u\frac{\partial u}{\partial x}+v\frac{\partial u}{\partial y}+\frac{\partial p}{\partial x}&=0\\ \frac{\partial v}{\partial t}+u\frac{\partial v}{\partial x}+v\frac{\partial v}{\partial y}+\frac{\partial p}{\partial y}&=0 \end{aligned} \tag{1}$$

To obtain characteristic structure of equations, a characteristic surface in the form of $f(x, y, t)=0$ is assumed. Using the kinematics relations for relating the partial derivatives to exact derivatives corresponding to the assumed surface, one obtains the following system of equations [32]:

$$\begin{bmatrix} f_t/\beta & f_x & f_y\\ f_x & \psi & 0\\ f_y & 0 & \psi \end{bmatrix}\begin{bmatrix} \mathrm{d}p\\ \mathrm{d}u\\ \mathrm{d}v \end{bmatrix}=\begin{bmatrix} 0\\ 0\\ 0 \end{bmatrix} \tag{2}$$

where the subscripts stand for the partial differentiation and ψ is defined as

$$\psi=\frac{\partial f}{\partial t}+u\frac{\partial f}{\partial x}+v\frac{\partial f}{\partial y} \tag{3}$$

For compatibility requirements of Equations (2), the determinant of coefficient matrix is set to zero; hence

$$\psi=0,\quad \psi=\frac{\beta}{f_t}(f_x^2+f_y^2) \tag{4}$$

We assumed the pseudo-velocity vector $\hat{V}=(u, v, 1)$ and normal vector to characteristic surface $\hat{n}=(\cos\varphi, \sin\varphi, n_t)$ alike compressible Euler equations [33], in which φ shows the wave direction.

DOI: 10.1002/fld

Expressing Equations (4) in terms of vectors $\hat{V}$ and $\hat{n}$, two types of characteristic surface corresponding to following relations are obtained:

$$\begin{aligned} \hat{V}\cdot\hat{n} &= 0 \\ \hat{V}\cdot\hat{n} &= \frac{\beta}{n_t} \end{aligned} \tag{5}$$

where $n_t = f_t/\sqrt{(f_x^2+f_y^2)}$ denotes the t-component of normal vector. By some mathematical operations, n_t takes the following form:

$$n_t = \frac{-(u\cos\varphi + v\sin\varphi) \pm \sqrt{(u\cos\varphi + v\sin\varphi)^2 + 4\beta}}{2} = n_1, n_2 \tag{6}$$

Regarding the dual roots of second relation in Equation (5) as a function of n_t, similar to compressible Euler equations, dual characteristic surfaces would exist. With straightforward mathematical operations it can be proven that the roots have always different signs. This depicts the growth of zones of influence and dependence around the pseudo-streamlines. The projection of normal vectors n_t in the x–y plane lies inside a unit circle. Two roots of Equation (6) for n_t denote the biplanes tangent to characteristic surfaces passing through a certain point and producing the Mach cones. Also, Mach conoid is tangent to Mach cone at each point passing through it. Along bicharacteristics, the characteristic surfaces are tangent to passing Mach cone. In fact, the characteristic paths corresponding to the first equation of (5) demonstrate the pseudo-pathlines and the second one corresponds to the pseudo-acoustic waves propagating within the incompressible flow field. To specify the wave paths on a Mach conoid, consider an assumed characteristic path on $f(x, y, t) = 0$. Taking $\mathrm{d}f/\mathrm{d}t = 0$ yields

$$\frac{\partial f}{\partial t} + \frac{\mathrm{d}x}{\mathrm{d}t}\frac{\partial f}{\partial x} + \frac{\mathrm{d}y}{\mathrm{d}t}\frac{\partial f}{\partial y} = 0 \tag{7}$$

From Equation (7) one obtains

$$n_t + (\mathrm{d}x/\mathrm{d}t)\cos\varphi + (\mathrm{d}y/\mathrm{d}t)\sin\varphi = 0 \tag{8}$$

Comparing Equations (5) and (8), the following relations would result:

$$\begin{aligned} n_t + (\mathrm{d}x/\mathrm{d}t)\cos\varphi + (\mathrm{d}y/\mathrm{d}t)\sin\varphi &= 0 \\ n_t + u\cos\varphi + v\sin\varphi &= \beta^2/(\rho n_t) \end{aligned} \tag{9}$$

Combining the above relations with each other results in the following:

$$(u - \mathrm{d}x/\mathrm{d}t)\cos\varphi + (v - \mathrm{d}y/\mathrm{d}t)\sin\varphi = \beta^2/(\rho n_t) \tag{10}$$

DOI: 10.1002/fld

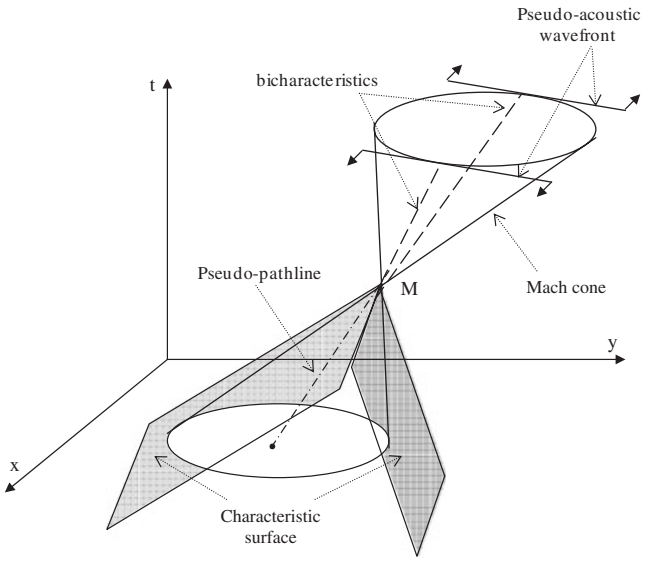

Figure 1. Characteristic structure for incompressible flow defined by artificial compressibility equations.

Therefore, the equations for characteristic paths take the form:

$$\begin{aligned} \frac{\mathrm{d}x}{\mathrm{d}t} &= u - \frac{\beta}{n_t}\cos\varphi \\ \frac{\mathrm{d}y}{\mathrm{d}t} &= v - \frac{\beta}{n_t}\sin\varphi \end{aligned} \tag{11}$$

where φ is the wave angle. By considering Equation (6), it is concluded that similar to compressible Euler equations, dual characteristic surfaces would exist, so that their corresponding tangential planes construct two Mach cones that extend from a certain point, namely domain of dependence and domain of influence (Figure 1). Similar approaches for two-dimensional characteristic structure of compressible Euler equations have been presented in References [24–26, 33].

As it is seen in Figure 1, for any angle in the range $0 \leqslant \varphi \leqslant 2\pi$ there exist two bicharacteristics. Unlike compressible Euler equations, here the cross-section of Mach cone with the x–y plane produces an ellipse (called Mach ellipse) having minor and major axes parallel to the coordinate axes. The compatibility relations are obtained from Equations (2) by the insertion of corresponding values of ψ from Equations (4), as

$$\begin{aligned} \frac{\beta}{n_t}\,\mathrm{d}u + \cos\varphi\,\mathrm{d}p &= 0 \\ \frac{\beta}{n_t}\,\mathrm{d}v + \sin\varphi\,\mathrm{d}p &= 0 \end{aligned} \tag{12}$$

Equations (12) are valid for both $n_t = n_1, n_2$, which show the governing compatibility relations along bicharacteristics.

DOI: 10.1002/fld

3. GOVERNING EQUATIONS

The Navier–Stokes equations for two-dimensional incompressible flows modified by the artificial compressibility can be expressed as

$$\iint_{\text{Vol.}} \frac{\partial \mathbf{W}}{\partial t}\,\mathrm{d}V + \oint_C (\mathbf{F}\,\mathrm{d}y - \mathbf{G}\,\mathrm{d}x) = \oint_C (\mathbf{R}\,\mathrm{d}y - \mathbf{S}\,\mathrm{d}x) \tag{13}$$

where

$$\mathbf{W} = \begin{bmatrix} p \\ u \\ v \end{bmatrix}, \quad \mathbf{F} = \begin{bmatrix} \beta u \\ u^2 + p \\ uv \end{bmatrix}, \quad \mathbf{G} = \begin{bmatrix} \beta v \\ uv \\ v^2 + p \end{bmatrix}, \quad \mathbf{R} = \frac{1}{Re}\begin{bmatrix} 0 \\ \partial u/\partial x \\ \partial v/\partial x \end{bmatrix}, \quad \mathbf{S} = \frac{1}{Re}\begin{bmatrix} 0 \\ \partial u/\partial y \\ \partial v/\partial y \end{bmatrix}$$

Here $\mathbf{W}$ is the vector of primitive variables, and $\mathbf{F}$, $\mathbf{G}$ and $\mathbf{R}$, $\mathbf{S}$ are convective and viscous flux vectors, respectively. The artificial compressibility parameter and Reynolds number are denoted by β and Re, respectively. The above equations have been nondimensionalized based on the following scalings:

$$(x, y) = (x^*/l^*, y^*/l^*), \quad t = \frac{t^*}{l^*/U_{\text{ref}}}, \quad (u, v) = (u^*/U_{\text{ref}}, v^*/U_{\text{ref}}), \quad p = \frac{p^* - p_{\text{ref}}}{\rho_{\text{ref}} U_{\text{ref}}^2} \tag{14}$$

The discretized form of Equation (13) is expressed as

$$A_{ij}\frac{\partial \mathbf{W}_{ij}}{\partial t} + \sum_{k=1}^{4} (\mathbf{F}\Delta y - \mathbf{G}\Delta x)_k = \sum_{k=1}^{4} (\mathbf{R}\Delta y - \mathbf{S}\Delta x)_k \tag{15}$$

where A_{ij} is the cell area.

4. NUMERICAL SCHEME

The characteristic relations derived in Section 2 can be used for flux treatment in finite volume or data reconstruction in finite difference methods. It is possible to select different characteristic paths and use their corresponding compatibility relations in order to estimate the cell interface values from previous time level. In this study, a new multidimensional characteristic-based (MCB) finite-volume method has been used for incompressible Navier–Stokes equations. The compatibility relations (12) are used to model convective fluxes, whereas the viscous fluxes are computed with conventional averaging method such as [34–36].

4.1. Convective fluxes

To evaluate the convective interface fluxes from previous time level quantities, four pseudo-acoustic waves with the projected propagation paths parallel to the x- and y-axes are selected. According to Figure 2, the intersection of local Mach cone corresponding to point M, on the two cells interfaces, with the x–y plane, demonstrates the real two-dimensional nature of information propagation.

DOI: 10.1002/fld

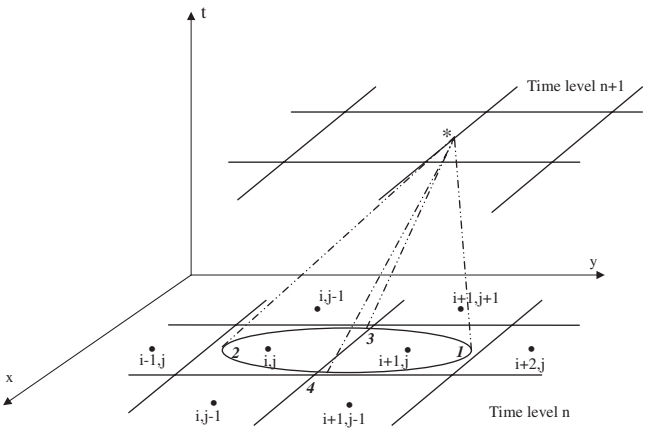

Figure 2. Intersection of local Mach cone with previous time level plane and proposed scheme stencil.

In order to take into account the physical behavior of domain of influence for point M, four pseudo-waves corresponding to wave angles $\varphi = 0, \pi/2, \pi, 3\pi/2$ are selected and Equations (12) are discretized along them. This is an alternative, such as done for compressible wave models introduced by Roe and coworkers [37–39]. It is possible to select different numbers and directions for waves and use their corresponding compatibility relations for evaluating interface values.

By selecting the above waves, to evaluate the convective flux at face $*$ in Figure 2, the following four compatibility relations are utilized (obtained from Equation (12) for different values of φ):

$$\begin{aligned}
&\frac{\beta}{n_t}\,\mathrm{d}u + \mathrm{d}p = 0 \quad \text{on } \varphi = 0 \text{ pseudo-acoustic wave}\\
&\frac{\beta}{n_t}\,\mathrm{d}u - \mathrm{d}p = 0 \quad \text{on } \varphi = \pi \text{ pseudo-acoustic wave}\\
&\frac{\beta}{n_t}\,\mathrm{d}v + \mathrm{d}p = 0 \quad \text{on } \varphi = \pi/2 \text{ pseudo-acoustic wave}\\
&\frac{\beta}{n_t}\,\mathrm{d}v - \mathrm{d}p = 0 \quad \text{on } \varphi = 3\pi/2 \text{ pseudo-acoustic wave}
\end{aligned} \tag{16}$$

Corresponding value of n_t for each wave angle is obtained from Equation (6). By inserting n_t values in Equations (16) and discretizing them, the following relations are obtained:

$$\begin{aligned}
&p^* - p_1 + A(u^* - u_1) = 0\\
&p^* - p_2 + B(u^* - u_2) = 0\\
&p^* - p_3 + C(v^* - v_3) = 0\\
&p^* - p_4 + C(v^* - v_4) = 0
\end{aligned} \tag{17}$$

DOI: 10.1002/fld

where A, B, C, D are defined as follows:

$$\begin{aligned} A &= \tfrac{1}{2}\left(u_1 - \sqrt{u_1^2+4\beta}\right) \\ B &= \tfrac{1}{2}\left(u_2 + \sqrt{u_2^2+4\beta}\right) \\ C &= \tfrac{1}{2}\left(v_3 - \sqrt{v_3^2+4\beta}\right) \\ D &= \tfrac{1}{2}\left(v_4 + \sqrt{v_4^2+4\beta}\right) \end{aligned} \tag{18}$$

p^*, u^* and v^* are the values at cell interface calculated by Equation (17) using flow properties at points $1, 2, 3$ and 4 (Figure 2) in the previous time level. Then they are used to determine convective fluxes at the cell interface. The value of u^* is determined from the first and second equations of Equations (17) and v^* is determined from third and fourth ones. The final value of p^* is assumed to be the arithmetic average of values obtained from two sets of equations (first–second and third–fourth in Equations (17)).

With this idea, a genuinely two-dimensional upwind algorithm, called MCB, has been developed for evaluation of flux vectors at the cell interfaces. In the first-order MCB scheme, flow properties at points 1, 2 are set to neighborhood cell values and for points 3, 4 interpolated from two cells containing assumed face. For second-order MCB scheme, the values of point 1 are interpolated from cells $(i+1, j)$ and $(i+2, j)$ and similarly for point 2 interpolated from cells (i, j) and $(i-1, j)$. Flow properties at point 3 are interpolated from cells $(i, j+1)$ and $(i+1, j+1)$ and for point 4 is also done similarly. The mentioned interpolations are similar to what has been done for two-dimensional CB schemes interpolations in the case of compressible Euler equations such as [24, 40]. We use one cell value for the first-order accuracy and averaging of two cell values for the second-order accuracy of the scheme as has been done in References [24, 40] in the case of compressible Euler equations. By using the flow values at points 3 and 4 in order to evaluate interface values at face $*$, we take into account the real two-dimensional nature of flow and do not assume any one-dimensional assumptions. It is obvious that the second-order scheme has a greater range of stability defined by the Courant–Friedrichs–Lewy (CFL) number, due to a wide range of interpolation points.

4.2. Viscous flux

To evaluate the viscous fluxes, one needs to compute flow variables derivatives at the cell interfaces as shown in Figure 3. For example, the first-order derivative at the side AB in Figure 3 is determined using the secondary cell ANBM as follows:

$$\begin{aligned} \left.\frac{\partial\phi}{\partial x}\right|_{AB} &= \frac{1}{S'}\iint_{S'}\frac{\partial\phi}{\partial x}\,\mathrm{d}S = \frac{1}{S'}\oint_{\partial S'}\phi\,\mathrm{d}y = \frac{1}{S'}\sum_{k=1}^{4}\phi_k\Delta y_k \\ &= \frac{1}{S'}[0.5(\phi_N+\phi_A)\Delta y_{AN} + 0.5(\phi_N+\phi_B)\Delta y_{NB} \\ &\quad + 0.5(\phi_B+\phi_M)\Delta y_{BM} + 0.5(\phi_M+\phi_A)\Delta y_{MA}] \end{aligned} \tag{19}$$

DOI: 10.1002/fld

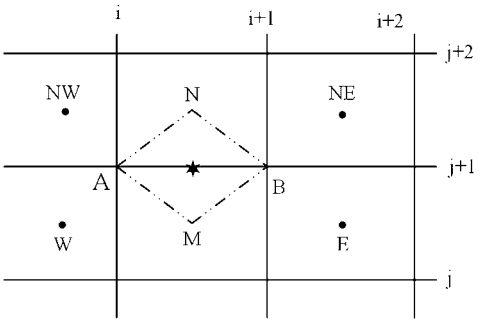

Figure 3. Pattern for discretization of the viscous terms.

where S' denotes the area of AMBN, also the ϕ_A and ϕ_B are calculated by averaging the neighboring cells. Here ϕ is a generic name standing for the flow variables.

4.3. Time integration

The spatially discretized equations form a set of coupled ordinary differential equations that are integrated in time by an explicit fourth-order Runge–Kutta scheme. The discretized equations are in the following form:

$$\frac{\partial \mathbf{W}}{\partial t} + \mathbf{Q} = 0 \tag{20}$$

After time discretization, one obtains

$$\begin{aligned}
\mathbf{W}^{(0)} &= \mathbf{W}^{(n)} \\
\mathbf{W}^{(1)} &= \mathbf{W}^{(0)} - \frac{\Delta t}{2}\mathbf{Q}^{(0)} \\
\mathbf{W}^{(2)} &= \mathbf{W}^{(0)} - \frac{\Delta t}{2}\mathbf{Q}^{(1)} \\
\mathbf{W}^{(3)} &= \mathbf{W}^{(0)} - \Delta t\mathbf{Q}^{(2)} \\
\mathbf{W}^{(4)} &= \mathbf{W}^{(0)} - \frac{\Delta t}{6}(\mathbf{Q}^{(0)} + 2\mathbf{Q}^{(1)} + 2\mathbf{Q}^{(2)} + \mathbf{Q}^{(3)})
\end{aligned} \tag{21}$$

where $\mathbf{Q}$ contains the convective and viscous terms. The maximum time step is determined from

$$\mathrm{CFL} = \left[\sqrt{u^2+v^2} + \sqrt{u^2+v^2+\beta}\right]\frac{\Delta t}{\Delta l} \tag{22}$$

Here, Δl is taken as the smallest distance between any cell center with its neighbor cell center. Applying MCB scheme, the permissible CFL numbers up to 2 have been used.

4.4. Boundary conditions

At solid walls, no-slip boundary conditions are imposed for velocities. The pressure on the wall is calculated from the normal-momentum equation.

DOI: 10.1002/fld

5. RESULTS AND DISCUSSION

The steady flow of an incompressible viscous fluid in a square cavity has been used for many years as a benchmark problem by researchers to test their new numerical schemes and solution

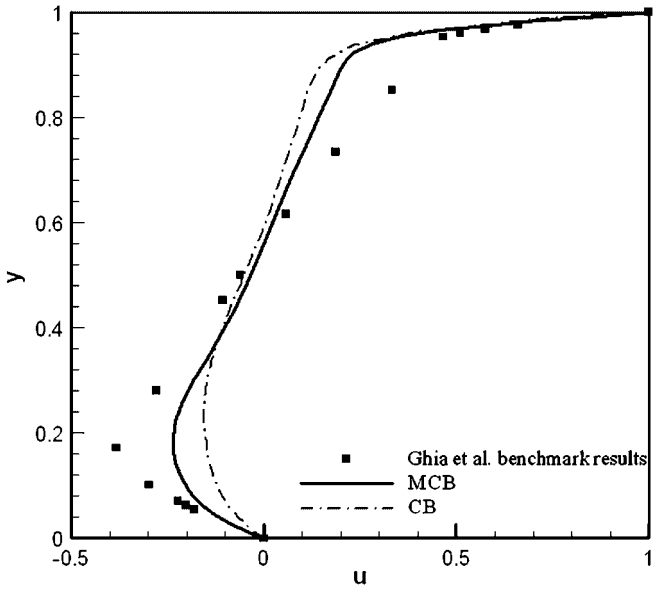

Figure 4. Comparison of results for u-velocity profile along vertical line passing through the cavity center obtained by first-order CB and MCB schemes at $Re = 1000$ on 40×40 grids.

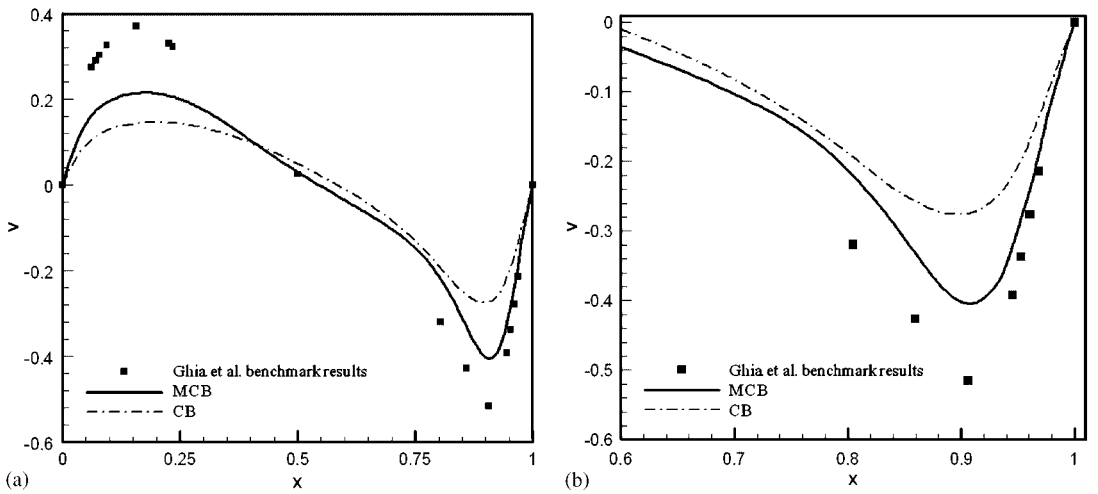

Figure 5. (a) Comparison of results for v-velocity profile along horizontal line passing through the cavity center obtained by the first-order CB and MCB schemes at $Re = 1000$ on 40×40 grids and (b) magnification of (a) for $x > 0.6$.

DOI: 10.1002/fld

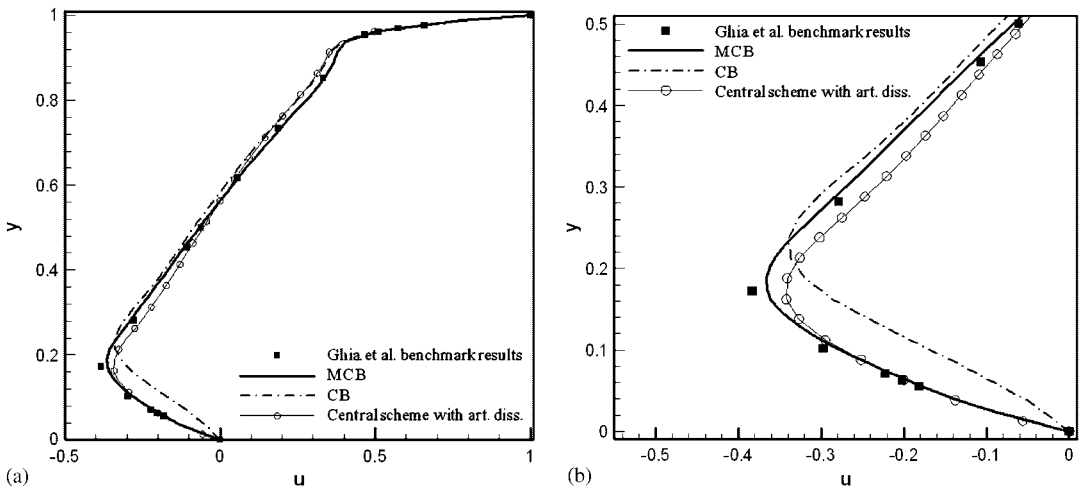

Figure 6. (a) Comparison of results for u-velocity profile along vertical line passing through the cavity center obtained by the central, second-order CB and second-order MCB schemes at $Re=1000$ on 40×40 grids and (b) magnification of (a) for $x<0$.

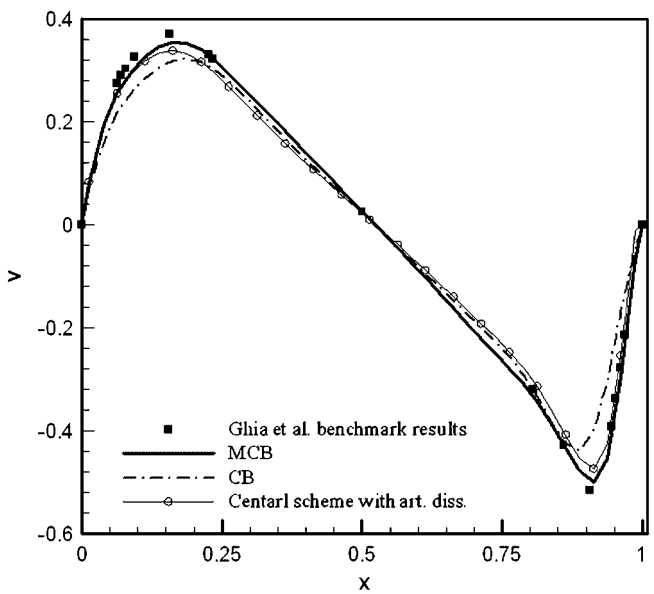

Figure 7. Comparison of obtained results for v-velocity profile along horizontal line passing through the cavity center using second-order CB and MCB schemes at $Re=1000$ on 40×40 grids.

methods [41–45]. To compare the accuracy and convergence rate of newly proposed MCB scheme with conventional methods, a series of tests were conducted at different Reynolds numbers. For example, the solution of steady flow at $Re=1000$ (based on moving wall velocity and cavity length)

DOI: 10.1002/fld

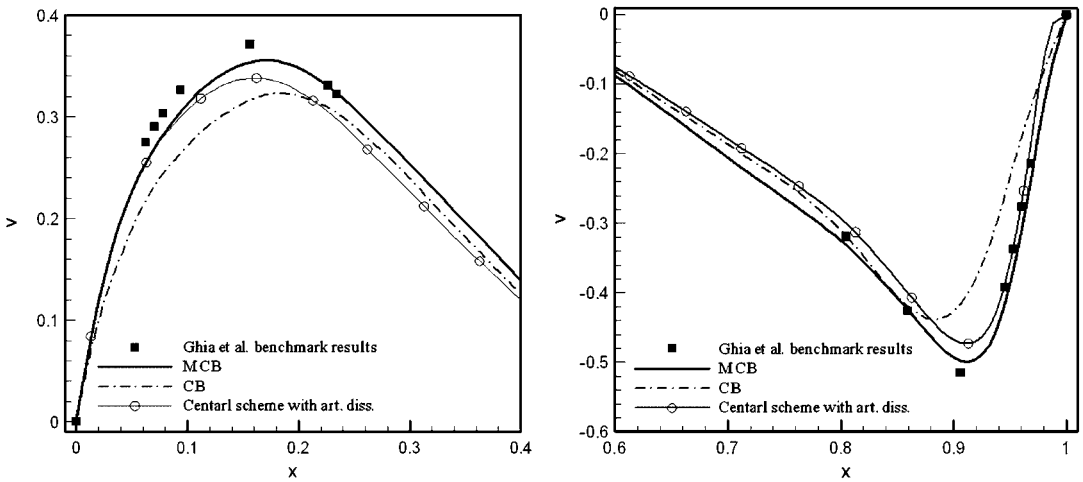

Figure 8. Magnified views of extremums in comparison of v-velocity profile along horizontal line passing through the cavity center using second-order CB and MCB schemes at $Re = 1000$ on 40×40 grids.

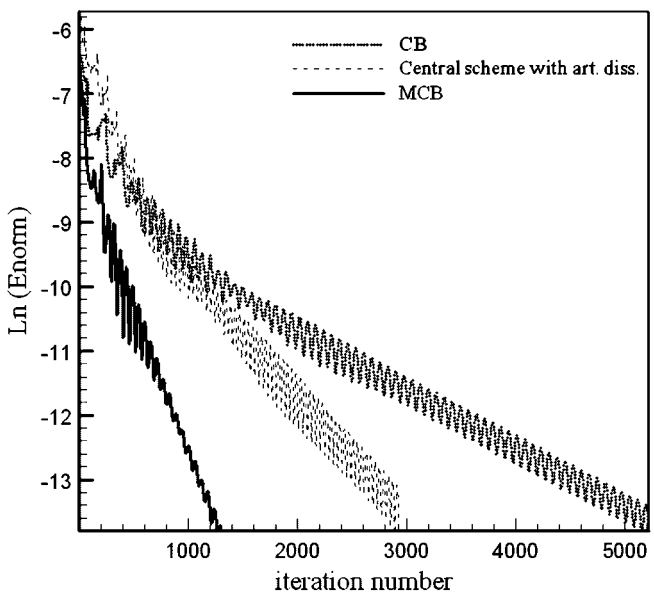

Figure 9. Comparison of convergence histories for three studied schemes, $Re = 1000$ on 40×40 grid.

on 40×40 uniform grid is presented. The artificial compressibility parameter has been considered 0.2 in all cases. Results obtained for u-velocity profile along vertical line and v-velocity profile along horizontal line passing through the center of the cavity using conventional CB scheme and MCB scheme are presented in Figures 4 and 5, respectively. Both schemes are used in first-order form and the obtained results are shown in comparison with Ghia *et al.* [42] benchmark solution.

DOI: 10.1002/fld

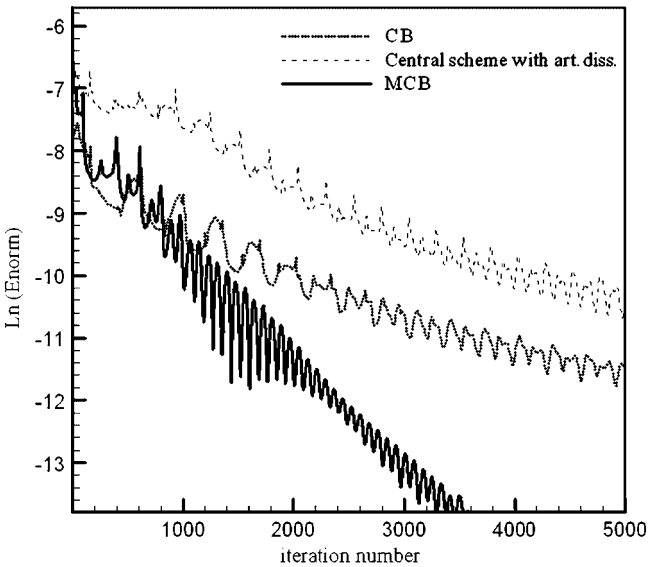

Figure 10. Comparison of convergence histories for three studied schemes, $Re = 5000$ on 80×80 grid.

Table I. Comparison of accuracy and convergence behavior of second-order MCB and CB schemes across the wide range of Reynolds numbers/grids.

		Max. permissible CFL		Number of iterations		U–y total dev. (%)		V–x total dev. (%)	
		CB	MCB	CB	MCB	CB	MCB	CB	MCB
$Re = 400$	20∗20 grid	0.9	1.6	3125	985	39.34	10.07	22.23	15.92
	40∗40 grid	0.8	1.6	12327	2534	12.93	5.32	10.45	3.68
$Re = 1000$	20∗20 grid	0.8	1.5	4380	2105	44.14	23.09	46.96	28.83
	40∗40 grid	0.9	1.6	14926	5667	24.13	5.62	18.81	8.02
	60∗60 grid	0.9	1.6	32247	9582	8.67	2.10	7.37	3.11
$Re = 5000$	40∗40 grid	0.8	1.6	Residuals stabilized at 2×10^{-3} after 14 800 iterations	23 186	32.01	20.60	49.44	35.80
	60∗60 grid	0.9	1.6	50401	45732	20.38	10.90	22.95	15.60
	80∗80 grid	0.9	1.7	Residuals stabilized at 1.4×10^{-4} after 100 000 iterations	70321	14.14	8.30	11.40	9.08
$Re = 10000$	60∗60 grid	0.8	1.5	92724	87364	28.84	14.92	39.69	28.11
	80∗80 grid	0.8	1.6	155208	135718	16.05	11.12	19.81	13.46
	100∗100 grid	0.9	1.5	195206	166136	9.44	8.85	8.56	7.74

DOI: 10.1002/fld

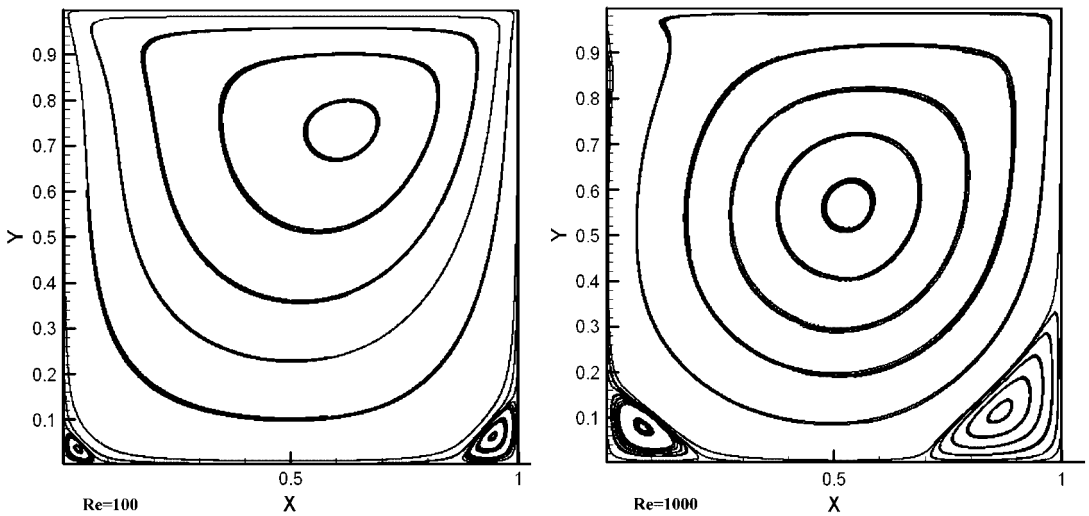

Figure 11. Streamlines of primary and secondary vortices, $Re = 100, 1000$ on 256×256 uniform grid.

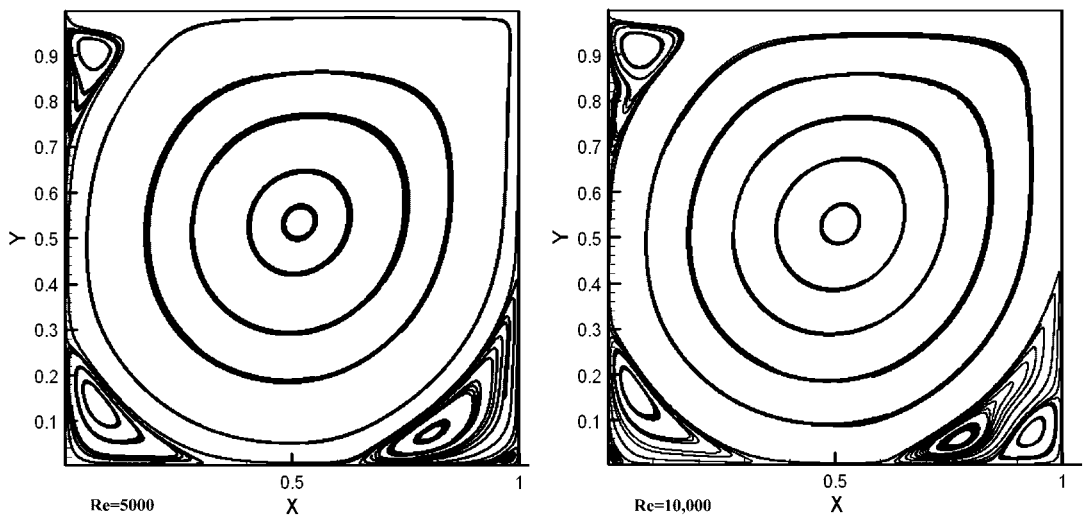

Figure 12. Streamlines of primary and secondary vortices, $Re = 5000, 10\,000$ on 256×256 uniform grid.

Same results for second-order CB and MCB schemes together with second-order central scheme plus artificial dissipation are presented in Figures 6–8. The enlarged views of the velocity profiles extremums are also shown. As it is shown in Figures 6–8, the proposed genuinely upwind scheme provides more accurate results than conventional one-dimensional CB method both in its first- and second-order forms on the same grid. Although the central scheme is genuinely second order in this case (due to the Cartesian grid), the second-order MCB scheme even presents more accurate results than the central scheme.

DOI: 10.1002/fld

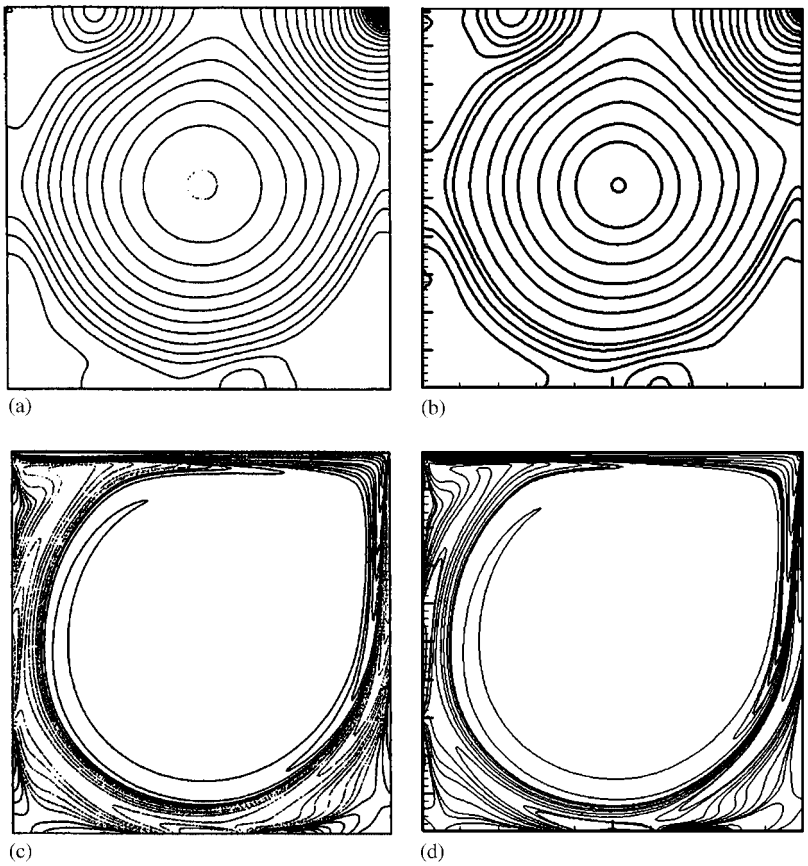

Figure 13. Pressure and vorticity contours for $Re=5000$ on 256×256 uniform grid: (a), (c) Bruneau and Saad [46] and (b), (d) second-order MCB.

In terms of convergence rate, it is found that the MCB scheme converges much more rapidly with respect to CB and central schemes. This is the remarkable advantage of MCB in comparison with CB scheme, where the substantial delays in convergence rate of CB scheme is observed [23, 30, 31]. The CB, central, and current MCB schemes have been tested for their convergence rate in which the MCB scheme presented a distinguished shorter iterations at a variety of Reynolds numbers. Figures 9 and 10 demonstrate typical convergence histories of three mentioned schemes at $Re=1000$ on 40×40 grid and $Re=5000$ on 80×80 grid, in which the MCB scheme presents the most rapid convergence. It should be noted that the three schemes have been run by their own maximum permissible CFL numbers. Error norm is defined as

$$\mathrm{ENORM}=\frac{\sqrt{\sum_{i=1}^{\mathrm{IM}}\sum_{j=1}^{\mathrm{JM}}(p_{i,j}^{n+1}-p_{i,j}^{n})^2}}{\mathrm{IM}\times\mathrm{JM}} \tag{23}$$

where IM and JM are the cell numbers along the x and y directions, respectively.

DOI: 10.1002/fld

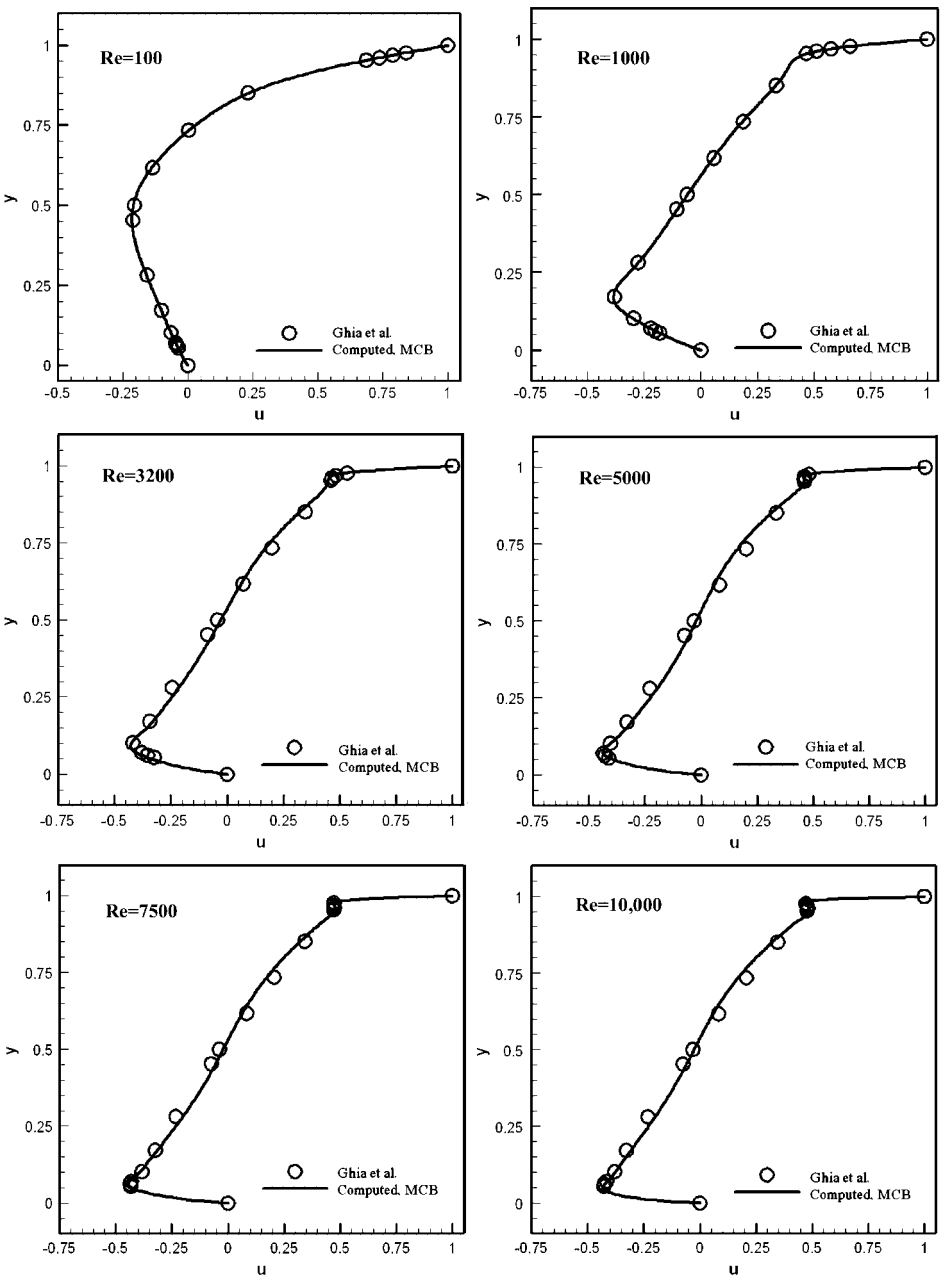

Figure 14. Computed u-velocity profiles along the vertical line passing through the cavity center at various Reynolds numbers on 256×256 uniform grid.

DOI: 10.1002/fld

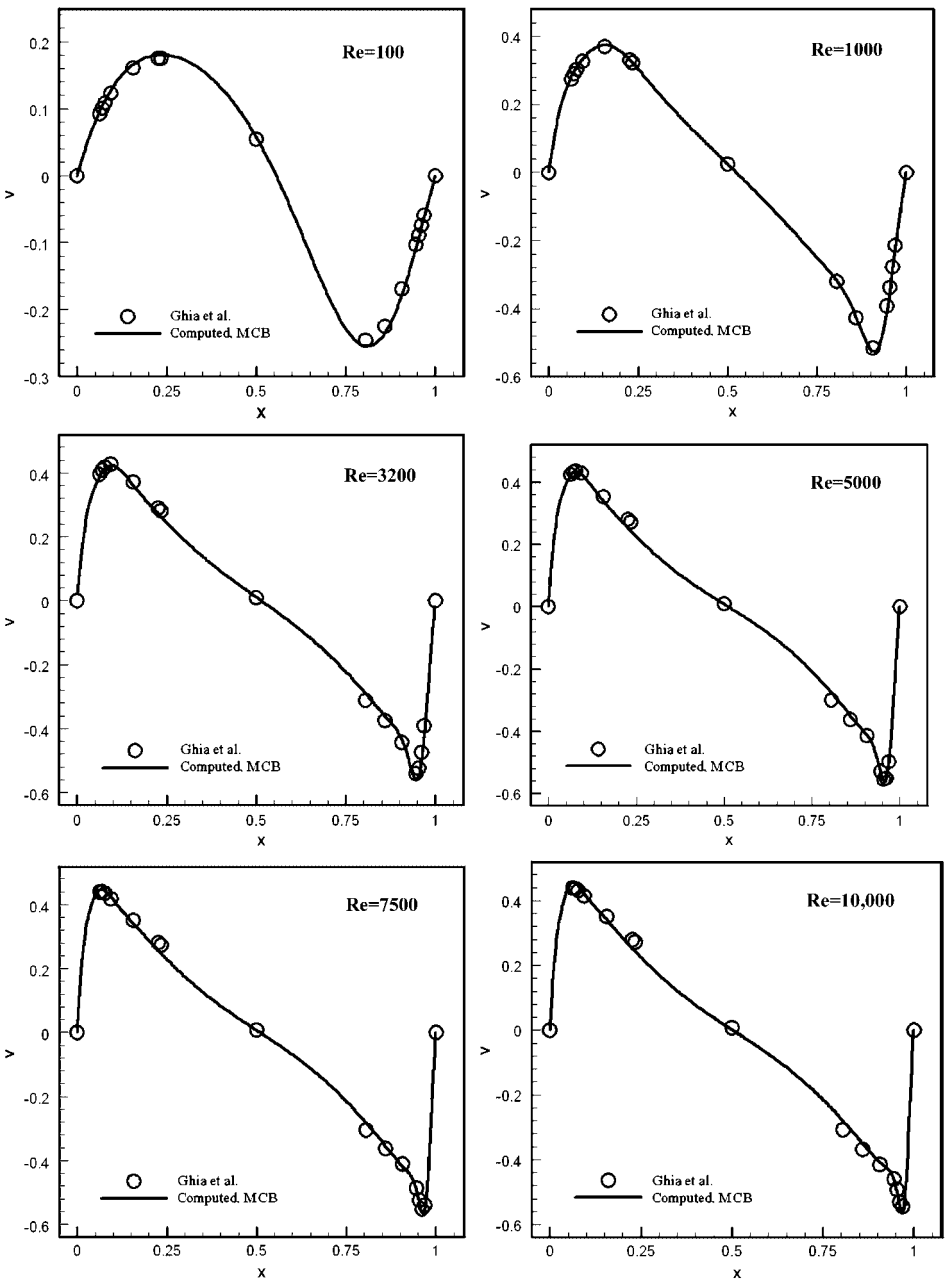

Figure 15. Computed v-velocity profiles along the horizontal line passing through the cavity center at various Reynolds numbers on 256×256 uniform grid.

DOI: 10.1002/fld

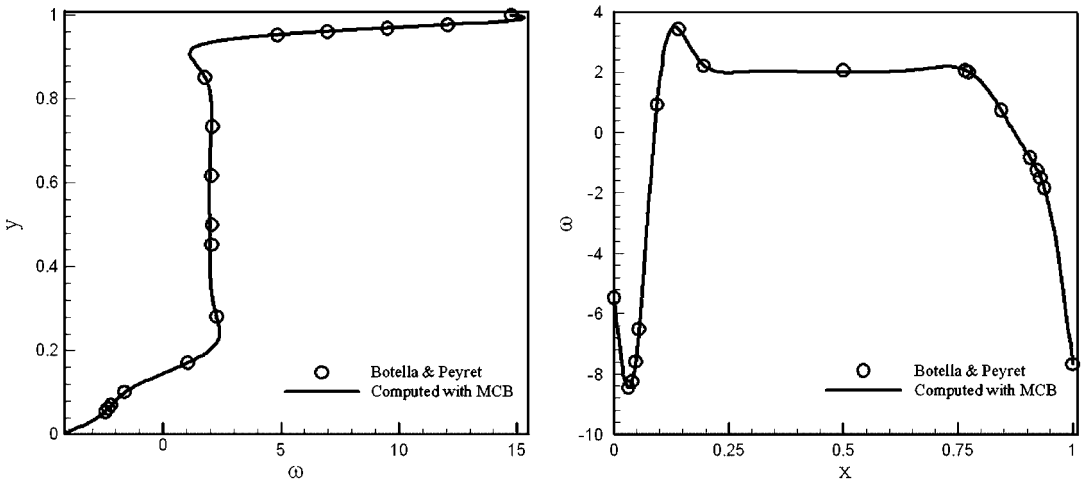

Figure 16. Comparison of results for vorticities along the vertical and horizontal lines passing through the cavity center at $Re=1000$ by second-order MCB scheme on 128×128 uniform grid and Botella and Peyret [47].

Utilizing second-order MCB scheme, the maximum permissible CFL number for $Re=1000$ on 40×40 uniform grid can be increased up to 2, while for second-order CB and central schemes it is limited to 0.9 and 1.7, respectively. Slow convergence behavior of CB scheme was observed in which the number of iterations needed for rms value of $\partial p/\partial t$ to reduce to 1×10^{-3} is 11 965 while for the central scheme and second-order MCB scheme it is 5938 and 4830, respectively. In order to compare the accuracy of second-order CB and MCB schemes across the range of Reynolds numbers/grids, the total deviation from the benchmark solution [42] is defined as follows:

$$\mathrm{DEV}=\frac{1}{N}\sum_{i=1}^{N}\left|\frac{\phi-\phi^*}{\phi^*}\right| \tag{24}$$

In which N is the number of points, ϕ^* is the benchmark data and ϕ is the corresponding result obtained by the scheme at the same value. Detailed analysis of second-order MCB in comparison with the second-order CB scheme in terms of accuracy, maximum permissible CFL number and the number of iterations across the wide range of Reynolds numbers/grids is carried out and the results are represented at Table I. The convergence criterion is satisfied when the rms value of $\partial p/\partial t$ reduces to 1×10^{-4}. As seen in Table I, the MCB scheme demonstrates remarkable advantages compared with CB in all aspects.

Figures 11 and 12 show streamlines of the 256×256 uniform grid solutions for a wide range of Reynolds numbers. The pressure and vorticity contours for $Re=5000$ are shown in Figure 13 comparing with Bruneau and Saad results [46]. It should be noted that the MCB scheme, which is based on multidimensional nature of flow and inherent upwinding for evaluating convection fluxes, requires no artificial viscosity even for high Reynolds numbers. Figures 14 and 15 present the u-velocity profile along a vertical line and v-velocity profile along a horizontal line passing through the cavity center. These profiles are in good agreement with the well-known benchmark results of Ghia *et al.* [42] shown by symbols in the figures.

DOI: 10.1002/fld

Botella and Peyret [47] have presented highly accurate Chebyshev collocation spectral vorticity data from inside the cavity along vertical and horizontal lines passing through the cavity center at $Re = 1000$. Comparing the results obtained by MCB scheme with their counterparts in Figure 16, it is found that the agreement with Botella and Peyret [47] is remarkable.

6. CONCLUSIONS

This study proposes a novel MCB upwind scheme for the simulation of incompressible viscous flows. The new MCB scheme uses multidimensional characteristic relations, which have been derived for the first time for incompressible flow equations modified by artificial compressibility. It takes into account the pseudo-acoustic wave propagation in multidimensional space. The proposed MCB scheme is used in finite-volume form to evaluate convective fluxes thereby to solve steady incompressible-driven cavity flow at a wide range of Reynolds numbers. It is concluded that the new MCB scheme provides more accurate results than conventional CB scheme in both first- and second-order form on the same grid in the case of driven cavity flow across the wide range of Reynolds number/grids. Since MCB employs characteristic based relations, it presents stable solutions and no artificial viscosity is required even at higher Reynolds numbers. The remarkable advantage of MCB with respect to CB and central schemes is its faster convergence rate, noting the slow convergence of CB schemes reported in the literature. The computed results using MCB scheme are in good agreement with the available benchmark solutions in literature.

ACKNOWLEDGEMENTS

This paper is an elicitation from the final report of the research thesis titled 'Extension of Characteristic Based Compressible Flow Schemes for Solution of Incompressible Navier–Stokes Equations' which is financially supported by research funds of University of Tabriz.

REFERENCES

1. Chorin AJ. A numerical method for solving incompressible viscous flow problems. *Journal of Computational Physics* 1967; **2**:12–26.
2. Kwak D, Kiris C, Kim CS. Computational challenges of viscous incompressible flows. *Computers and Fluids* 2005; **34**:283–299.
3. Farmer J, Martinelli L, Jameson A. Fast multigrid method for solving incompressible hydrodynamic problems with free surface. *AIAA Journal* 1994; **32**:1175–1182.
4. Rogers SE, Kwak D. Steady and unsteady solutions of the incompressible Navier–Stokes equations. *AIAA Journal* 1991; **29**:603–610.
5. Liu C, Zheng X, Sung CH. Preconditioned multigrid methods for unsteady incompressible flows. *Journal of Computational Physics* 1998; **139**:35–57.
6. Kallinderis Y, Ahn HT. Incompressible Navier–Stokes method with general hybrid meshes. *Journal of Computational Physics* 2005; **210**:75–108.
7. Yuan L. Comparison of implicit multigrid schemes for three-dimensional incompressible flows. *Journal of Computational Physics* 2002; **177**:134–155.
8. Drikakis D, Govatsos PA, Papantonis DE. A characteristic based method for incompressible flows. *International Journal for Numerical Methods in Fluids* 1994; **19**:667–685.
9. Drikakis D. A parallel multiblock characteristic based method for three-dimensional incompressible flows. *Advances in Engineering Software* 1996; **26**:111–119.
10. Drikakis D, Iliev OP, Vassileva DP. A nonlinear multigrid method for the three-dimensional incompressible Navier–Stokes equations. *Journal of Computational Physics* 1998; **146**:301–321.

DOI: 10.1002/fld

11. Zhao Y, Zhang B. A high-order characteristics upwind FV method for incompressible flow and heat transfer simulation on unstructured grids. *Computer Methods in Applied Mechanics and Engineering* 2000; **190**:733–756.
12. Tai CH, Zhao Y. Parallel unsteady incompressible viscous flow computations using an unstructured multigrid method. *Journal of Computational Physics* 2003; **192**:277–311.
13. Tai CH, Zhao Y, Liew KM. Parallel computation of unsteady three-dimensional incompressible viscous flow using an unstructured multigrid method. *Computers and Structures* 2004; **82**:2425–2436.
14. Tai CH, Zhao Y, Liew KM. Parallel-multigrid computation of unsteady incompressible viscous flows using a matrix-free implicit method and high-resolution characteristics-based scheme. *Computer Methods in Applied Mechanics and Engineering* 2005; **194**:3949–3983.
15. Tai CH, Zhao Y, Liew KM. Parallel computation of unsteady incompressible viscous flows around moving rigid bodies using an immersed object method with overlapping grids. *Journal of Computational Physics* 2005; **207**:151–172.
16. Siong K, Zhao CY. Numerical study of steady/unsteady flow and heat transfer in porous media using a characteristics-based matrix-free implicit FV method on unstructured grids. *International Journal of Heat and Fluid Flow* 2004; **25**:1015–1033.
17. Shapiro E, Drikakis D. Artificial compressibility, characteristics-based schemes for variable density, incompressible, multi-species flows. Part I. Derivation of different formulations and constant density limit. *Journal of Computational Physics* 2005; **210**:584–607.
18. Shapiro E, Drikakis D. Artificial compressibility, characteristics-based schemes for variable density, incompressible, multi-species flows. Part II. Multigrid implementation and numerical tests. *Journal of Computational Physics* 2005; **210**:608–631.
19. Drikakis D, Goldberg U. Wall-distance-free turbulence models applied to incompressible flows. *International Journal of Computational Fluid Dynamics* 1998; **10**:241–253.
20. Mallinger F, Drikakis D. Instability in three-dimensional unsteady stenotic flows. *International Journal of Computational Heat Fluid Flow* 2002; **23**:657–663.
21. Drikakis D, Smolarkiewicz PK. On spurious vortical structures. *Journal of Computational Physics* 2001; **172**: 309–325.
22. Drikakis D. Bifurcation phenomena in incompressible sudden expansion flows. *Physics of Fluids* 1997; **9**:76–87.
23. Neofytou P, Drikakis D. Non-Newtonian flow instability in a channel with a sudden expansion. *Journal of Non-Newtonian Fluid Mechanics* 2003; **111**:127–150.
24. Osnaghi C. Explicit evaluation of discontinuities in 2D unsteady flows solved by the method of characteristics. *Eleventh International Conference on Numerical Methods in Fluid Dynamics*, Williamsburg, Virginia. Lecture Notes in Physics, vol. 323, 1988.
25. Zannetti L, Colasurdo G. Unsteady compressible flow: a computational method consistent with the physical phenomena. *AIAA Journal* 1981; **19**:852–856.
26. Zannetti L, Moretti G. Numerical experiments on the leading-edge flowfield. *AIAA Journal* 1982; **20**(12): 1668–1673.
27. Parpia IH. Finite-difference method-of-characteristics scheme for the equation of Gasdynamics. *AIAA Journal* 1991; **29**(4):567–571.
28. Roe PL. Discrete models for the numerical analysis of time dependent multidimensional gas dynamics. *Journal of Computational Physics* 1986; **63**(2):458–476.
29. Lacor C, Hirsch Ch. Genuinely upwind algorithms for the multidimensional Euler equations. *AIAA Journal* 1992; **30**(1):56–63.
30. Neofytou P, Drikakis D, Leschziner MA. Study of Newtonian and non Newtonian fluid flow in a channel with a moving indentation. In *Proceedings of the IMA Conference on Cardiovascular Flow Modelling with Application to Clinical Medicine*, Sajjadi S, Nash G, Rampling M (eds), Salford, U.K., 1998, Clarendon Press: Oxford, 1999.
31. Neofytou P. Revision of the characteristics-based scheme for incompressible flows. *Journal of Computational Physics* 2007; **222**:475–484.
32. Razavi SE. Far field boundary conditions for computation of compressible aerodynamic flows. *Ph.D. Thesis*, Department of Mechanical Engineering, McGill University, Montreal, Canada, 1995.
33. Zacrow MJ, Hoffman JD. *Gas Dynamics*, vol. II. Wiley: New York, 1976.
34. Kallinderis Y. A finite volume Navier–Stokes algorithm for adaptive grids. *International Journal for Numerical Methods in Fluids* 1992; **15**:193–217.
35. Kallinderis JG. Baron JR. In *The Finite Volume Approach for the Navier–Stokes Equations*, Chapter 4, Murthy TKS, Brebbia CA (eds). Elsevier: Amsterdam, 1990.

DOI: 10.1002/fld

36. Ekaterinaris JA. High-order accurate numerical solutions of incompressible flows with the artificial compressibility method. *International Journal for Numerical Methods in Fluids* 2004; **45**:1187–1207.
37. Roe PL. Discrete models for the numerical analysis of time dependent multidimensional gas dynamics. *Journal of Computational Physics* 1986; **63**(2):458–476.
38. Paillere H, Deconinck H, Struijs R, Roe PL, Measaros LM, Muller JD. Computations of inviscid compressible flows using fluctuation splitting on triangular meshes. *AIAA-93-3301-CP*, 1993.
39. Rumsey C, Van Leer B, Roe PL. Effect of a multi-dimensional flux function on the monotonicity of Euler and Navier–Stokes computations. *AIAA-91-4530-CP*, 1991.
40. Sauerwein H. The method of characteristics for the three-dimensional unsteady magnetofluid dynamics of a multi-component medium. *Journal of Fluid Mechanics* 1966; **25**:17–41.
41. Altas I, Burrage K. A high accuracy defect-correction multigrid method for the steady incompressible Navier–Stokes equations. *Journal of Computational Physics* 1994; **114**:227–233.
42. Ghia U, Ghia KN, Shin CT. High-Re solutions for incompressible flow using the Navier–Stokes equations and a multigrid method. *Journal of Computational Physics* 1982; **48**:387–411.
43. Gupta MM. High accuracy solutions of incompressible Navier–Stokes equations. *Journal of Computational Physics* 1991; **93**:343–359.
44. Erturk E, Gokcol C. Fourth order compact formulation of Navier–Stokes equations and driven cavity flow at high Reynolds numbers. *International Journal for Numerical Methods in Fluids* 2006; **50**:421–436.
45. Zhang J. Numerical simulation of 2D square driven cavity using fourth order compact finite difference schemes. *Computers and Mathematics with Applications* 2003; **45**:43–52.
46. Bruneau CH, Saad M. The 2D lid-driven cavity problem revisited. *Computers and Fluids* 2006; **35**:326–348.
47. Botella O, Peyret R. Benchmark spectral results on the lid-driven cavity flow. *Computers and Fluids* 1998; **27**:421–433.

DOI: 10.1002/fld